

# **The influence of the mesoporous TiO<sub>2</sub> scaffold on the performance of methyl ammonium lead iodide (MAPI) perovskite solar cells: charge injection, charge recombination and solar cell efficiency relationship**

**Alba Matas Adams · Jose Manuel Marin-Beloqui · Georgiana Stoica; Emilio Palomares**

*<sup>a</sup>Institute of Chemical Research of Catalonia (ICIQ), Avda. Paisos Catalans, 16, Tarragona E-43007, Spain*

*<sup>b</sup>ICREA, Passeig Lluís Companys, 18, Barcelona, E-08020, Spain*

---

Methyl Ammonium Lead Iodide (MAPI) perovskite solar cells have achieved over 20% light-to-energy conversion efficiency with the use of a thin mesoporous layer of TiO<sub>2</sub> as a scaffold for the MAPI. Although other solar cell configurations have also been reported, so far only those containing mesoporous TiO<sub>2</sub> (mpTiO<sub>2</sub>) have achieved such performance. Herein we describe an exhaustive study of the effects, on the MAPI solar cell performance, of different synthetic routes to achieve nanocrystalline TiO<sub>2</sub> nanoparticles that are used to fabricate the mpTiO<sub>2</sub> layer. Furthermore, we also measured the interfacial charge transfer dynamics to elucidate the device function–charge recombination kinetics relationship in the different types of synthesised mpTiO<sub>2</sub>. Our results show that the choice of the chemical properties of the mpTiO<sub>2</sub> layer is of utmost importance to achieve high solar-to-energy conversion efficiencies with remarkable effects on the measured charge carrier recombination kinetics.

## **Introduction**

The research of earth abundant and inexpensive materials for solar cells such as MAPI,<sup>1,2</sup> SnS<sup>3</sup> and CZTS<sup>4</sup> is attracting much attention and holds the promise to fill the gap of the terawatt solar energy production.<sup>5</sup>

In less than 5 years the reported efficiency for MAPI perovskite solar cells has arrived to overpass 20% under standard conditions (100 mW cm<sup>-2</sup> sun-simulated 1.5 AM G).<sup>6</sup>

Although the interest in MAPI, as a photoactive material, in solar cells has resulted in multiple solar cell configurations,<sup>2</sup> with solar cell efficiencies superior to other related energy conversion devices such as dye sensitized solar cells, organic solar cells and quantum dot solar cells, the most utilised configuration is the one that uses mesoporous TiO<sub>2</sub> (mpTiO<sub>2</sub>) as a scaffold and/or contact electrode. In fact, the best reported efficiencies have been published with the following device configuration:

FTO/dTiO<sub>2</sub>/mTiO<sub>2</sub>/MAPI or MAPIC/HTM/Au where FTO is fluorine doped tin oxide, dTiO<sub>2</sub> is a thin and dense layer of TiO<sub>2</sub>, mpTiO<sub>2</sub> is the mesoporous layer of TiO<sub>2</sub>, MAPI or MAPIC is methyl ammonium lead iodide without or with chloride, respectively, HTM is the hole transport material and Au is the gold metal contact.

Mesoporous TiO<sub>2</sub> has been widely used in different areas such as catalysis,<sup>8</sup> sensing<sup>9</sup> and energy.<sup>10</sup> In the latter area of research, energy, TiO<sub>2</sub> is of paramount importance in so-called Grätzel solar cells<sup>11</sup> or dye sensitized solar cells (DSSCs) with an outstanding number of reports on the properties of the mpTiO<sub>2</sub> and its effects on the DSSC performance.<sup>12-14</sup> In contrast, in MAPI solar cells the number of such studies is scarce for several reasons, including the considerable recent discovery of MAPI solar cells and the fact that MAPI solar cells can also be constructed without the use of mpTiO<sub>2</sub> with a noteworthy efficiency.<sup>15,16</sup> Nonetheless, there are important scientific questions that are still under debate in relation with the role of the nanocrystalline TiO<sub>2</sub> nanoparticles and, hence, the mpTiO<sub>2</sub> layer over the MAPI device function. For example, taking into account that MAPI solar cells also work well using mpAl<sub>2</sub>O<sub>3</sub> as a scaffold and Al<sub>2</sub>O<sub>3</sub> is a well-known wide band-gap insulator, it is not clear if it is really necessary an efficient electron transfer reaction from the MAPI perovskite material to the TiO<sub>2</sub> conduction band, TiO<sub>2</sub> CB, (so-called charge injection in parallelism with the charge transfer from the dye excited state to the TiO<sub>2</sub> CB in DSSC) or if the electron accumulation at the mpTiO<sub>2</sub> plays a role in the MAPI solar cell voltage at all.

In this work we aim to study how different mpTiO<sub>2</sub> layers fabricated using different synthetic routes<sup>12</sup> effect a change on the MAPI solar cell parameters (short circuit current,  $I_{sc}$ , open circuit voltage,  $V_{oc}$ , fill factor, FF and the overall efficiency,  $\eta$ ). The synthetic routes differ under the synthetic pH conditions, leading to an acidic route and a basic route and their respective acidic or basic TiO<sub>2</sub> pastes used to fabricate the mpTiO<sub>2</sub>. Moreover, we examined the electrical differences of the different MAPI perovskite solar cells in terms of charge density (defined as the total accumulated

charge at the solar cell) as a function of light bias (cell voltage due to externally applied light at different and controlled light intensities) and its relation with the capacitance and carrier recombination lifetime measured under solar cell working conditions.

## Experimental Section

### Nanocrystalline TiO<sub>2</sub> nanoparticle (ncTiO<sub>2</sub>) synthesis

The colloids of titanium dioxide nanoparticles were obtained using the same precursor (titanium isopropoxide), but different peptidization agents were used to modify the surface charge. Two different synthetic routes were followed as previously reported by Hore *et al.*<sup>12</sup>

#### Acidic route

The acidic preparation of TiO<sub>2</sub> nanocrystalline nanoparticles consisted of mixing 20 mL of anhydrous titanium isopropoxide (Sigma Aldrich© 97%) under an argon atmosphere with 5.5 mL of glacial acetic acid (Panreac©) and stirring for 10 minutes.

In a separate Erlenmeyer, 120 mL of a 0.1 M nitric acid solution (Scharlau, 69.5%) in distilled water was degassed with argon.

The TiO<sub>2</sub> colloidal solution was injected dropwise at room temperature while stirring.

The final mixture was stirred vigorously under argon at 1500 rpm for 10 minutes, and finally heated in air for 8 hours at 80 °C followed by room temperature cooling overnight.

Next, the solution was filtered at room temperature using a 0.45 µm syringe filter.

To allow the ncTiO<sub>2</sub> to grow into the desired particle size, 5% in weight of the ncTiO<sub>2</sub> solution was autoclaved at 220 °C for 12 hours and later allowed to cool down to room temperature. The obtained particle sizes were between 15 and 20 nm.

The colloids were dispersed with a 60 second cycle burst using a sonic probe horn, and concentrated to 12.5% in TiO<sub>2</sub> weight to prepare the acidic mpTiO<sub>2</sub> paste for the MAPI perovskite solar cell fabrication.

#### Basic route

A similar procedure was followed for the basic peptidization, but instead of mixing the titanium isopropoxide with acetic acid, the 20 mL were injected dropwise into a 0.1 M solution of tetramethylammonium hydroxide (Sigma Aldrich©, 25 wt% in H<sub>2</sub>O) in

distilled water previously degassed with argon. The solution was vigorously stirred at 1500 rpm for 10 minutes and then heated at 80 °C, 500 rpm for 8 h.

Next, the solution was left to cool down overnight, filtered as mentioned above and recovered.

For the basic route, the procedure to grow the nanoparticles is alike the acidic route but the autoclave temperature is set to 180 °C.

In both cases, to form the titanium dioxide pastes from the ncTiO<sub>2</sub>, we added 6.2 w% of poly(ethylene oxide) (Sigma Aldrich©, molecular weight ( $M_w$ )  $\approx$  300 000) to the final suspension.

## **Nanocrystalline TiO<sub>2</sub> nanoparticle characterization**

The nanocrystalline TiO<sub>2</sub> particles were characterized using XRD (X-ray powder diffraction), TEM (transmission electron microscopy), nitrogen isotherms (Brunauer–Emmett–Teller) and Z potential measurements as shown.

Powder XRD was measured in a Bruker© AXS D8 Advance diffractometer equipped with a Cu tube, a Ge (111) incident beam monochromator, and a Vantec-1 PSD. Data were recorded in the range of 5–70° 2 $\theta$  with an angular step size of 0.016° and a counting time of 6 seconds per step.

Transmission Electron Microscopy (TEM) was carried out in a JEOL JEM-1011 microscope operating at 100 kV and equipped with a SIS Megaview III CCD camera. 5  $\mu$ L of the sample suspended in ethanol were placed on a carbon-coated copper grid followed by evaporation under ambient conditions.

The zeta potential ( $\zeta$ -potential) was measured using a NanoSizer (MALVERN© Nano-ZS) using dynamic light scattering (DLS) and the Smoluchowski equation. All measurements were performed at 25 °C.

Nitrogen isotherm (BET) measurements were carried out at 77 K on a Quantachrome Autosorb© iQ analyser. Prior to the analysis, the samples were degassed in a vacuum at 300 °C for 5 h. The BET theory was applied to calculate the total surface area.

## **MAPI perovskite solar cell fabrication and characterization**

The device presents the following architecture: FTO/d-TiO<sub>2</sub>/mp-TiO<sub>2</sub>/MAPI/OMeTAD/gold, and for its preparation a thin (50 nm) and dense titanium oxide layer (d-TiO<sub>2</sub>) was deposited by spin-coating onto Fluorine doped Tin Oxide glass (FTOs) with a resistance of 8  $\Omega$  cm<sup>-2</sup> as previously described.<sup>17</sup>

To homogenize this layer, the substrates were immersed in a 40 mM TiCl<sub>4</sub> solution at 70 °C for 30 minutes and annealed at 500 °C for 20 minutes.

Next, the mesoporous titanium oxide layer (mp-TiO<sub>2</sub>) was spin-coated, and in this case, three different pastes of titanium oxide were used: commercial paste (Ti nanoxide HT/SP Solaronix©), acidic paste and basic paste, in different proportions of paste:

ethanol, to obtain a mesoporous TiO<sub>2</sub> layer of 400 nm. The substrates were then heated at 325 °C for 30 minutes, 375 °C for 5 minutes, 450 °C for 15 minutes and 500 °C for 30 minutes.

For the MAPI perovskite preparation, methyl ammonium iodide (MAI) synthesized as described previously<sup>18</sup> was mixed with lead chloride (PbCl<sub>2</sub>) (Sigma Aldrich©, 98%) in a 3 : 1 molar ratio in DMF (anhydrous dimethyl formamide) and deposited over the different mp-TiO<sub>2</sub> films in a glovebox ([H<sub>2</sub>O] < 0.1 ppm and [O<sub>2</sub>] < 100 ppm) at 2000 rpm for 60 seconds.

Next, the film was annealed at 100 °C for 1 hour.

The Hole Transport Material (HTM) spiro-OMeTAD (1-Material©) was dissolved in chlorobenzene (70 mg mL<sup>-1</sup>). Bis(trifluoromethane)-sulfonimide lithium salt (520 mg mL<sup>-1</sup>) and 4-tertbutylpyridine were used as chemical additives.

For all different devices we maintained identical spin-coating conditions.

Finally, an 80 nm layer of gold was evaporated as the anode by thermal evaporation at a pressure close to  $1 \times 10^{-6}$  mbar.

## Photo-induced characterization

Several techniques have been used to characterise either mpTiO<sub>2</sub>/MAPI and mpTiO<sub>2</sub>/MAPI/OMeTAD thin films or complete MAPI perovskite solar cells.

Picosecond–nanosecond Time Correlated Single Photon Counting (ps–ns TCSPC) was used to estimate charge injection and measure the radiate recombination lifetime. The system used was an Edinburgh Instruments© LifeSpec-II spectrometer with a PMT detector and a laser excitation source with a nominal wavelength of 470 nm and an IR (Instrument Response) measured at FWHM (full width at half maximum) of 400 ps.

Photo-induced charge recombination kinetics in thin films were measured using a home-build L-TAS system (Laser Transient Absorption Spectroscopy) that consists of a Nd-YAG excitation source in line with an optical parametric oscillator (OPO) to tune the excitation wavelength with a laser pulse energy of 75 μJ cm<sup>-2</sup>. The probe wavelength is a 150 W lamp that is filtered through two monochromators from Dongwoo Optron (DM500i model) positioned in front and behind the sample holder. The signal is recorded using an InGaAs photodiode for the IR region.

Photo-induced differential charging (PIDC) was used to register the charge accumulated at the solar cell under different light biases. The PIDC technique was used as described before.<sup>12</sup>In brief, PIDC uses the photo-induced transient photocurrent (PIT-PC) decay and the PIT-PV decay to calculate the solar cell capacitance assuming two caveats: (1) the charge losses at short circuit in the solar cell under illumination are

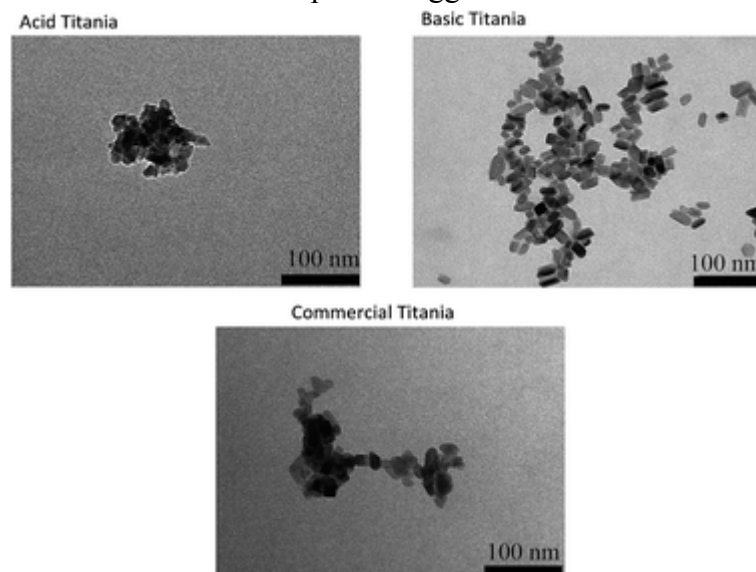
negligible and (2) the solar cell  $I_{sc}$  value is linear with the increase of sun-simulated light intensity. The first caveat can be tested by measuring PIT-PC in the dark and under 1 sun conditions and is found that there are no critical differences in both decays. The second caveat can be tested by measuring the MAPI solar cell under different light intensity conditions and registering the  $I_{sc}$ . The relationship between  $I_{sc}$  and light intensity (LI) must be close to  $\alpha = 1$  where  $\alpha$  is the exponential factor in the power law relationship  $P \propto LI^\alpha$

The photo-induced transient photovoltage (PIT-PV) was measured using a rig of white LEDs plus a nanosecond PTI GL-3300 N<sub>2</sub> dye laser.<sup>19</sup> Once the MAPI solar cell voltage has reached equilibrium, for a given light bias, a short laser pulse given by the N<sub>2</sub> dye laser produced a small change in  $V_{oc}$  (usually less than 20 mV). The original  $V_{oc}$  is restored after the N<sub>2</sub>dye laser pulse. The generated voltage decay, thus, represents a small  $\Delta V$  at a given light bias that can be directly correlated with the device charge measured at the same given light bias ( $V_{oc}$ ).

## Results and discussion

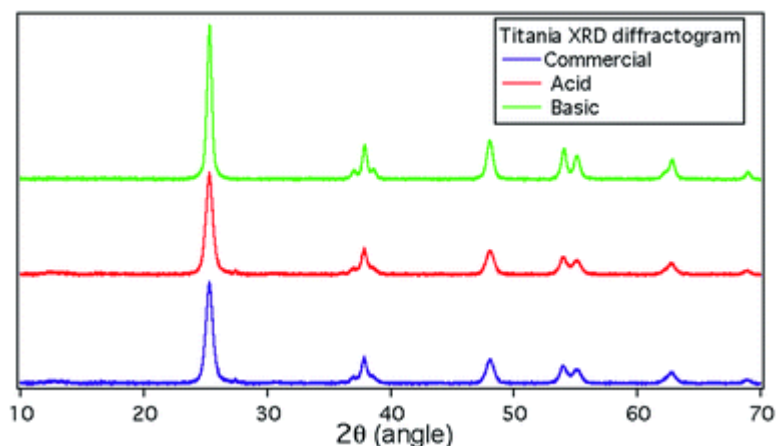
### Nanocrystalline TiO<sub>2</sub> nanoparticles (ncTiO<sub>2</sub>)

Fig. 1 illustrates the TEM (Transmission Electron Microscopy) images of the acidic, the basic and a commercial sample of ncTiO<sub>2</sub> particles. As can be seen, the acidic route leads to smaller ncTiO<sub>2</sub> with a more spherical shape than that presented in the case of the basic nanoparticles that have a rod-like shape and bigger size.



**Fig. 1** TEM images of ncTiO<sub>2</sub> obtained from different synthetic routes. The scale bar is 100 nm.

The X-ray diffraction (XRD) measurements (Fig. 2) show clear diffraction peaks at 2 theta angles ( $2\theta$ ) of  $25^\circ$  and  $48^\circ$  indicating the  $\text{TiO}_2$  anatase phase, in good agreement with the standard spectrum (JCPDS: 84-1286). Moreover, it can be seen that for the basic  $\text{ncTiO}_2$  the diffraction pattern is more resolved into sharp peaks in contrast with the acidic  $\text{ncTiO}_2$  samples but in this case is due to the small size of the acidic  $\text{TiO}_2$  nanoparticles.



**Fig. 2** XRD measurements of  $\text{ncTiO}_2$  acidic samples (red),  $\text{ncTiO}_2$  basic samples (green) and commercial  $\text{ncTiO}_2$  (purple).

We carried out further analysis of the samples measuring the zeta potential and the surface area. The zeta potential is a key measurement to evaluate the different charges at the surface of the  $\text{ncTiO}_2$  particles. Table 1 shows the different properties of the  $\text{ncTiO}_2$  samples studied in the present work.

**Table 1**  $\text{ncTiO}_2$  characterisation parameters<sup>a</sup>

	Size (nm)	$S_{\text{BET}}$ ( $\text{m}^2 \text{g}^{-1}$ )	$V_{\text{pore}}$ ( $\text{cm}^3 \text{g}^{-1}$ )	PSD (nm)	$Z_{\text{pot}}$ (mV)
<sup>a</sup> $S_{\text{BET}}$ = surface area measurement, $V_{\text{pore}}$ = pore volume, PSD = pore size distribution, $Z_{\text{pot}}$ = zeta potential, and Com = commercial sample.					
Acidic	10–20	92	0.2	8.46	–14.6
Basic	15–30	49	0.11	9.33	–24.8
Com	10–20	85	0.48	22.6	–3.53

Thus, as can be seen from Fig. 1 and 2, as well as from the parameters listed in Table 1, there are important differences between the  $\text{ncTiO}_2$  particles depending on the synthetic route. For example, the different zeta potentials can be correlated with

different pH values for the mpTiO<sub>2</sub> paste as demonstrated before.<sup>20</sup> The acidic paste with a −14.6 mV will correspond to a pH value of 6.5, while in the case of the basic paste, −24.8 mV corresponds to a pH of 7.5, which is neutral pH.

Once the ncTiO<sub>2</sub> was characterised we prepared mpTiO<sub>2</sub> thin films alike the ones which will be used for the fabrication of the solar cells and performed the initial characterization of two of the interfacial charge transfer reactions that occur in the solar cell as detailed in the next point.

### Charge injection in mpTiO<sub>2</sub>/MAPI thin films and charge recombination in mpTiO<sub>2</sub>/MAPI and mp/TiO<sub>2</sub>/OMeTAD thin films

On the one hand, we measured the charge injection from the MAPI perovskite into the TiO<sub>2</sub> CB using TCSPC as detailed in the Experimental section. The TCSPC is commonly used to scrutinize the radiative recombination lifetime in MAPI and MAPIC thin films<sup>21,22</sup> and has been used to evaluate the radiative charge recombination order.<sup>23</sup> Here we used the TCSPC measurements to measure the changes on the MAPI perovskite radiative recombination lifetime. Fig. 3 illustrates the different photoluminescence decays of the different mpTiO<sub>2</sub>/MAPI films.

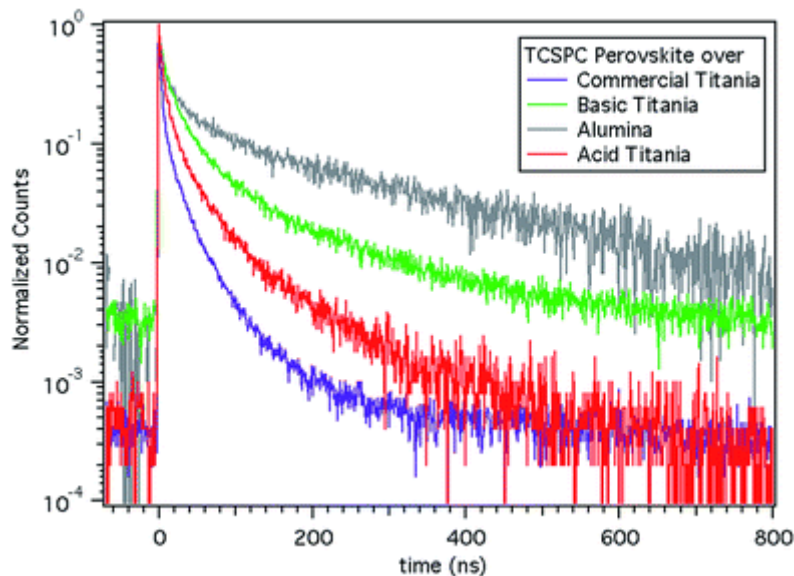


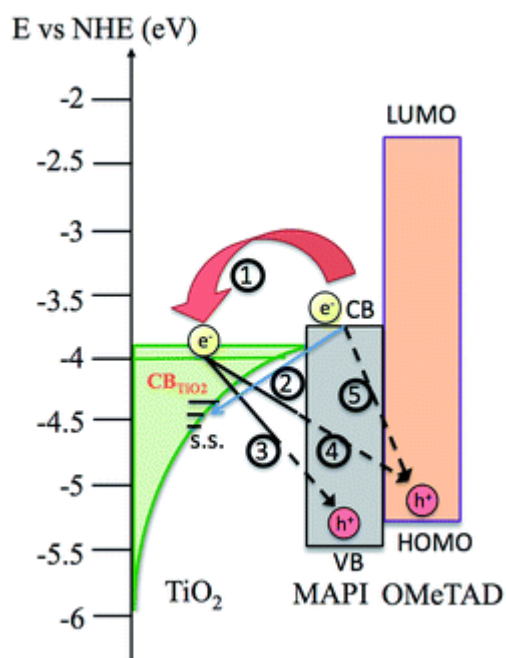
**Fig. 3** Normalised photoluminescence decays measured after excitation at  $\lambda = 470$  nm under nitrogen and monitoring at 750 nm.

As can be appreciated the MAPI perovskite radiative recombination lifetime is greatly affected upon the different mpTiO<sub>2</sub> films. It is worthy to mention that we have also used mpAl<sub>2</sub>O<sub>3</sub> for comparison purposes and all films have equivalent absorbance at the excitation wavelength ( $\lambda_{\text{ex}} = 470$  nm).



The slower decay lifetime of the pastes corresponds to the basic mpTiO<sub>2</sub> with a value of  $\tau_1 = 47$  ns and  $\tau_2 = 6$  ns, in contrast with the acidic mpTiO<sub>2</sub> that has a decay lifetime of  $\tau_1 = 30$  ns and  $\tau_2 = 5$  ns. These values appear to be faster than those values reported for other MAPI films.<sup>23</sup>

On the other hand, we used IR L-TAS to measure the interfacial charge recombination in mpTiO<sub>2</sub>/MAPI/spiro-OMeTAD films. Upon light excitation the MAPI perovskite generates free carriers (electrons and holes) and can transfer an electron to the TiO<sub>2</sub> CB or, alternatively, can transfer an electron to a TiO<sub>2</sub> surface state (TiO<sub>2</sub>-ss). While the latter case results in a charge loss, the former case can lead to electrical work if the charge is transported efficiently to the contact. However, it is also likely that the electron can undergo back electron transfer to the MAPI perovskite or to the spiro-OMeTAD film. Last but not least, it is also feasible that upon light excitation and carrier generation an electron can be directly transferred from the MAPI perovskite CB to the HTM spiro-OMeTAD. Scheme 1 shows a representation of the interfacial charge transfer described above. Needless to say that we have not included other charge transfer reactions (*i.e.*: radiative and non-radiative charge transfer reactions within the MAPI perovskite) to simplify the graphical representation.

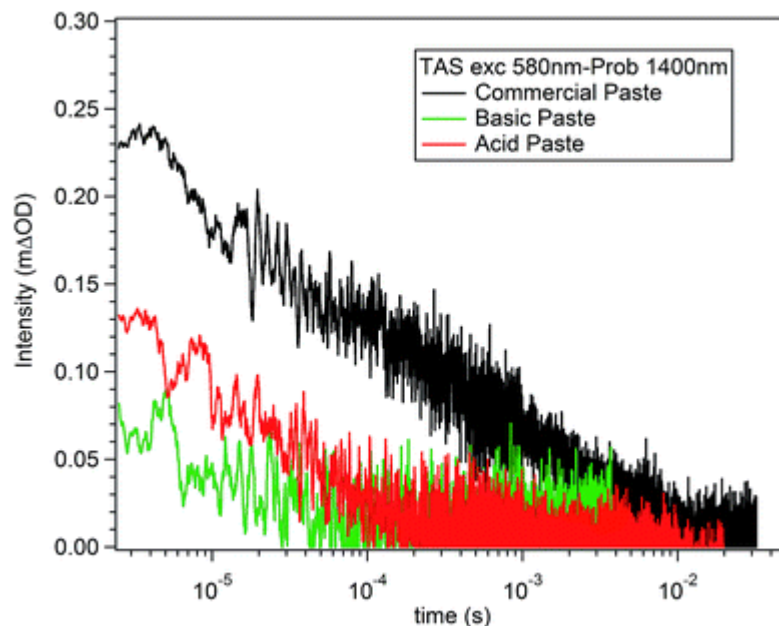


**Scheme 1** Interfacial charge transfer reactions upon light excitation in mpTiO<sub>2</sub>/MAPI/spiro-OMeTAD. (1) Electron injection from the MAPI perovskite CB to the TiO<sub>2</sub> CB. (2) Charge transfer from the MAPI perovskite CB to the TiO<sub>2</sub> surface states. (3) Back-electron transfer from the TiO<sub>2</sub> to the MAPI perovskite VB (valence band). (4) Back-electron transfer from the

TiO<sub>2</sub> to the spiro-OMeTAD and (5) electron transfer from the MAPI perovskite to the spiro-OMeTAD.

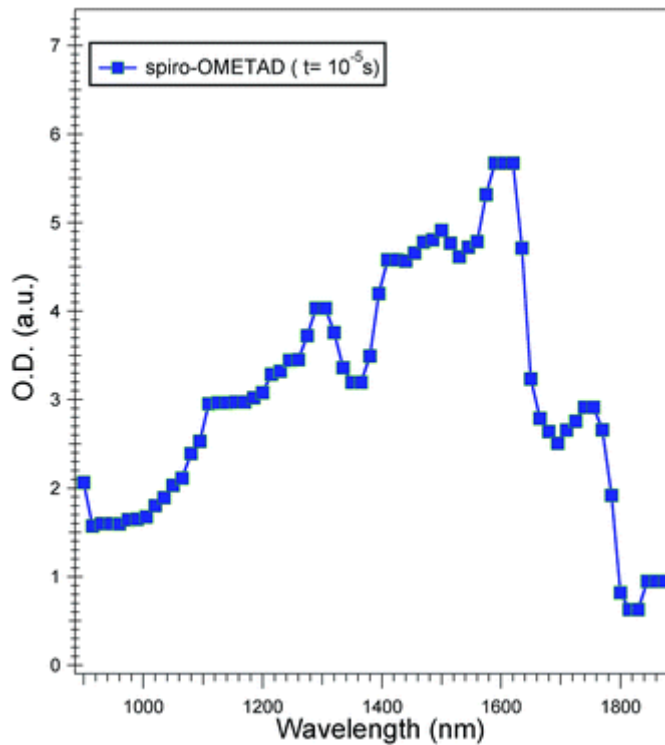
The interfacial electron transfer reaction (4) shown in Scheme 1 is still under debate as it implies that electrons must be transported through the perovskite material to recombine with holes at the HTM, in this case the spiro-OMeTAD.<sup>24</sup> This process can be possible if charges have excellent mobility at the MAPI perovskite and also may occur if the perovskite overlayer on top of the mpTiO<sub>2</sub> presents micropores where the spiro-OMeTAD can penetrate and get closer to the TiO<sub>2</sub>. In any case, early work by Moser and co-workers has already measured this electron transfer reaction, which supposes a non-radiative carrier recombination pathway that minimised the solar cell efficiency.<sup>25</sup> Yet, we must consider that these measurements and the ones described herein below are registered under dark conditions (without any light bias) and may differ from charge transfer reactions under light irradiation conditions.<sup>26</sup>

Fig. 4 shows the IR L-TAS interfacial charge recombination reaction, reaction 4 in Scheme 1, for our different mpTiO<sub>2</sub>/MAPI/spiro-OMeTAD thin films. We registered the measurements at  $\lambda_{\text{probe}} = 1400$  nm that corresponds to the wavelength near the maximum absorption of the spiro-OMeTAD positive polarons (spiro-OMeTAD<sup>+</sup>) as reported before.<sup>24</sup> Fig. 5 illustrates the IR L-TAS spectrum of the mpTiO<sub>2</sub>/MAPI/spiro-OMeTAD upon excitation at  $\lambda_{\text{ex}} = 580$  nm under nitrogen at 25° C.



**Fig. 4** Photo-induced interfacial charge recombination decays for the mpTiO<sub>2</sub> acidic (red), mpTiO<sub>2</sub> basic (green) and the mpTiO<sub>2</sub> commercial pastes with the MAPI perovskite and the spiro-OMeTAD layers alike in a functional solar cell. The excitation wavelength was  $\lambda_{\text{ex}} = 580$  nm and the probe wavelength was  $\lambda_{\text{probe}} = 1400$  nm.

---



**Fig. 5** Photo-induced IR-LTAS spectrum of a mpTiO<sub>2</sub>/MAPI/spiro-OMeTAD film (mpTiO<sub>2</sub>commercial) registered after 10 microseconds of laser excitation (laser power 70  $\mu\text{J cm}^{-2}$ ) at  $\lambda_{\text{ex}} = 580$  nm under ambient conditions.

---

As can be seen in [Fig. 4](#), the most striking observation is the low signal amplitude for the basic mpTiO<sub>2</sub> sample in comparison with the acidic mpTiO<sub>2</sub> and the commercial mpTiO<sub>2</sub> paste. As all samples have alike absorption at 580 nm, this result implicates that for the basic mpTiO<sub>2</sub> there is a much less yield of electron injection from the MAPI perovskite to the TiO<sub>2</sub> CB. In contrast, the signal amplitude for the commercial

mpTiO<sub>2</sub>/MAPI/spiro-OMeTAD film denotes a greater yield for the electron injection (reaction 1 at [Scheme 1](#)) process.

The IR L-TAS measurements are in good agreement with the measurements carried out using TCSPC and shown in [Fig. 3](#), where the mpTiO<sub>2</sub>/MAPI basic film shows the slowest radiative recombination decay for TiO<sub>2</sub> samples and the electron injection in this particular film is not efficient. Thus, we can establish that the order for efficient electron injection in our different mpTiO<sub>2</sub> films is commercial > acidic > basic ncTiO<sub>2</sub> nanoparticles. Moreover, another important feature that can be seen in [Fig. 4](#) is the different decay half-lifetimes (measured at the decay half maximum of its signal amplitude) for the acidic and the commercial mpTiO<sub>2</sub>/MAPI/spiro-OMeTAD films. The former has a  $\tau_{1/2} = 26 \mu\text{s}$  and the latter has a  $\tau_{1/2} = 170 \mu\text{s}$ , respectively. As the laser power intensity was maintained constant and the MAPI perovskite absorption at the excitation wavelength was alike the first hypothesis for the observed difference in decay lifetimes is that the electrons at the acidic mpTiO<sub>2</sub> are deeply trapped while in the commercial mpTiO<sub>2</sub> the electrons are in shallow traps and can more easily migrate to the surface.

To complete our study, we now turned into the fabrication and characterization of the MAPI perovskite solar cells using the different mpTiO<sub>2</sub> films.

## MAPI perovskite solar cell characterization

We fabricate the MAPI perovskite solar cells as detailed at the Experimental section. [Fig. 6](#) shows the measured IV curves (current vs. voltage) under standard 1 sun measuring conditions (100 mW cm<sup>-2</sup> sun-simulated 1.5 AM G spectrum).

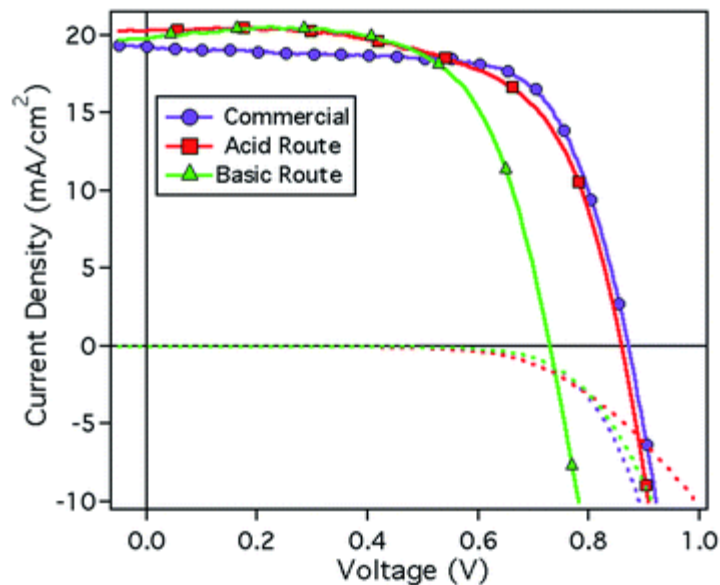


**Fig. 6** The current vs. voltage curves measured under 1 sun (1.5 AM G sun simulated irradiation, lines with markers) and under dark conditions in reverse bias with an integration time of 8 seconds and a delay time of 0 seconds. The solar cells have an area of 0.25 cm<sup>2</sup>.

The most relevant parameters from the measured MAPI perovskite solar cells are listed in [Table 2](#). The solar cells fabricated with the basic mpTiO<sub>2</sub> show almost identical  $J_{sc}$  ( $\approx 20$  mA cm<sup>-2</sup>), however, the  $V_{oc}$  (730 mV) is systematically lower in these devices. On the other hand, the acidic mpTiO<sub>2</sub> film shows almost alike performance as the commercial TiO<sub>2</sub> paste.

**Table 2** Most relevant parameters for the MAPI perovskite solar cells measured in this work<sup>a</sup>

	$J_{sc}$ (mA)	$V_{oc}$ (mV)	FF (%)	$\eta$ (%)	$R_s$ ( $\Omega$ )	$R_{sh}$ ( $\Omega$ )
<sup>a</sup> $J_{sc}$ = photocurrent density, $V_{oc}$ = open circuit voltage, FF = fill factor, $\eta$ = efficiency, $R_s$ = series resistance, $R_{sh}$ = shunt resistance.						
Basic	19.8	733	66.56	9.62	9	$4.25 \times 10^4$
Acidic	20.10	870	63.25	11.06	22	$1.3 \times 10^5$
Com	19.35	870	69.14	11.64	6.6	$8.1 \times 10^4$

To study further the reasons for the differences between the acidic and the basic mpTiO<sub>2</sub> films in MAPI perovskite solar cells we carried out, as detailed below, photo-induced time resolved advanced spectroscopy such as PIDC and PIT-PV.

## Photo-induced differential charging (PIDC) and photo-induced transient photo-voltage (PIT-PV)

The PIDC technique has been previously applied in OPV and QDSC (quantum dot solar cells) and more recently in MAPI perovskite solar cells to measure the charge density at different light biases.<sup>17</sup> As can be seen in [Fig. 7](#), the PIDC data at different light biases lead to a different exponential distribution of the charges. The PIDC data are the result of the accumulated charges at the different materials including the mpTiO<sub>2</sub>, the MAPI perovskite and the HTM.

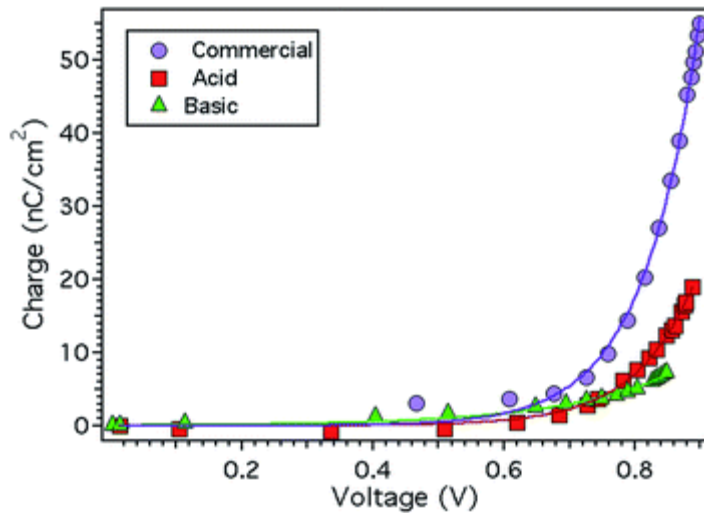


**Fig. 7** Charge measured using PIDC at different light biases for the different mpTiO<sub>2</sub> MAPI perovskite solar cells.

Previously, mpTiO<sub>2</sub> based MAPI perovskite solar cell PIDC was correlated with the electronic charge in the solar cell and, moreover, it was possible to obtain the recombination current value  $J_{\text{rec}}$  for the devices with good agreement with the measured  $J_{\text{sc}}$ . However, the  $J_{\text{rec}}$  values were only meaningful when the fastest component of the PIT-PV decay was considered.

We carried out the PIT-PV measurements (Fig. 8), as described before, leaving the MAPI solar cell under different illumination intensities to stabilize its  $V_{\text{oc}}$ .

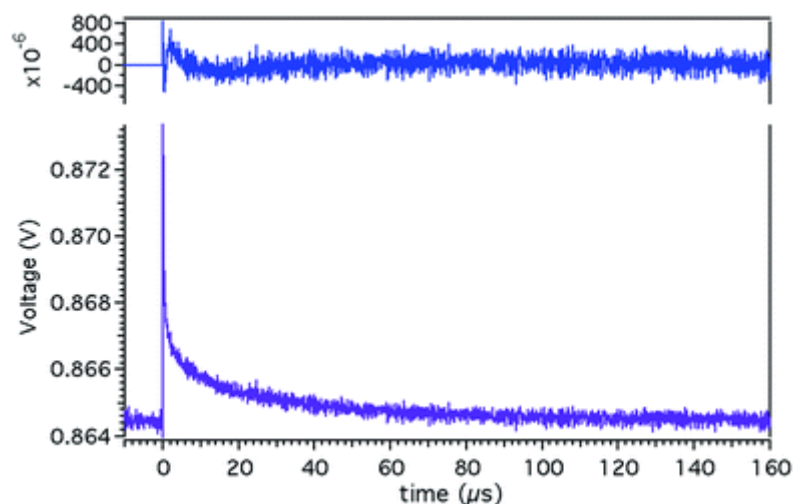


**Fig. 8** The PIT-PV decay at 1 sun (solar cell  $V_{oc} = 0.870$  V) for the MAPI solar cells fabricated using the commercial mpTiO<sub>2</sub>. The top figure shows the residual plot for the decay fitting to a bi-exponential equation.

For all MAPI solar cells, independent of the mpTiO<sub>2</sub> used, the PIT-PV decay cannot be fitted to a single mono-exponential equation but to a double-exponential equation instead. These results are in good agreement with previous measurements.<sup>17,19</sup>

In Fig. 9, we compare the fastest component of the PIT-PV decay at the same charge measured by PIDC.

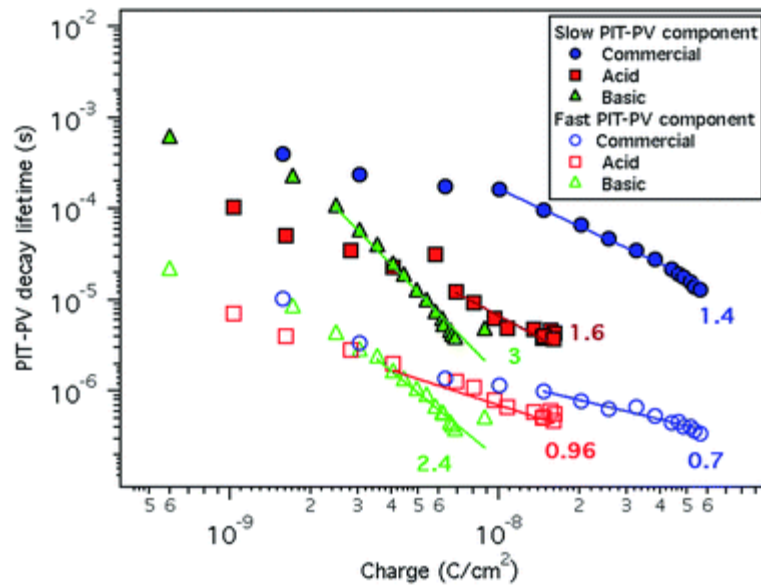


**Fig. 9** Charge vs. PIT-PV decay lifetimes. Filled and empty symbols correspond to the slow and the fast decay components, respectively.

As can be seen, the slowest decay lifetime corresponds to the commercial mpTiO<sub>2</sub> MAPI perovskite solar cells in clear contrast with the basic TiO<sub>2</sub> based devices.

On the one hand, the faster lifetime component of the decay for the basic mpTiO<sub>2</sub> MAPI perovskite solar cells can explain the lower  $V_{oc}$  observed for these devices. This fast component is related to the electronic charge in the solar cell and the carrier recombination kinetics. Moreover, the slope of the charge vs. the decay lifetime for the basic mpTiO<sub>2</sub> ( $\alpha = 2.4$ ) implicates that small changes in the light bias leads to a greater increase of the decay kinetics in comparison with the acidic or the commercial mpTiO<sub>2</sub> MAPI perovskite solar cells, which present an  $\alpha = 0.96$  and  $\alpha = 0.7$ , respectively. On the other hand, the charge vs. decay lifetime for the acidic

mpTiO<sub>2</sub> MAPI perovskite solar cell is not much different when compared to the commercial mpTiO<sub>2</sub> device, which is in good agreement with the measured  $V_{oc}$  (Fig. 6).

## Conclusions

Overall, we have demonstrated that different synthetic routes to achieve nanocrystalline TiO<sub>2</sub> nanoparticles lead to substantial differences in the solar-to-energy conversion efficiency of mesoporous TiO<sub>2</sub>/MAPI based solar cells. The differences observed are more accentuated in the solar cell open-circuit voltage value. A complete study of the charge transfer reactions in complete devices illustrates that for the solar cells based on the mpTiO<sub>2</sub> from the basic route the electron transfer from the MAPI conduction band to the TiO<sub>2</sub> conduction band is less favoured. This can be understood in terms of the TiO<sub>2</sub> conduction band energy position. It is well established that the TiO<sub>2</sub> conduction band can be shifted towards higher energy values, which makes the charge transfer less favourable. For example, in DSSCs the use of pyridine in the liquid electrolyte shifts the TiO<sub>2</sub> CB and decreases the electron injection from the dye excited state (and hence the device photocurrent). In MAPI solar cells, since MAPI can transport effectively electrons and holes within the same material, there is no need for mesoporous TiO<sub>2</sub> to transport the electrons to the contact. Thus, even though the electron transfer process is less efficient in the basic TiO<sub>2</sub> it is still feasible to achieve high currents alike in Al<sub>2</sub>O<sub>3</sub>mesoporous based MAPI solar cells.<sup>27</sup> This result is further confirmed by L-TAS where the decay amplitude, which is related to the population of polarons in the spiro-OMETAD as a result of the charge transfer process between the MAPI and the spiro-OMETAD, is also much lower for the basic mpTiO<sub>2</sub>/MAPI solar cell.

Moreover, the analysis of the charges at the solar cells, under different illumination conditions using PIDC, shows that for a given voltage, close to sun-simulated illuminations of 1 sun, the acidic and the basic mpTiO<sub>2</sub> show similar values in contrast to the commercial mpTiO<sub>2</sub>/MAPI that has higher charge density. In other types of solar cells,<sup>28</sup> the accumulated charge is related to the splitting of the quasi Fermi levels in the different materials that lead to the solar cell junction. The energy difference between the quasi Fermi levels is directly related to the solar cell open-circuit voltage. Hence, the more the charge accumulated, the greater the difference in energy between the quasi Fermi levels and higher is the  $V_{oc}$ . Furthermore, the analysis of the PIT-PV decay kinetics (Fig. 9) indicates that it is faster for the basic TiO<sub>2</sub>, when comparing the data at the same charge density, and these faster kinetics are related to the lower measured  $V_{oc}$  because the analysis of the charge densities for the acidic and the basic TiO<sub>2</sub> (Fig. 7) shows that they are almost identical despite the larger  $V_{oc}$  measured for the acidic TiO<sub>2</sub>. Thus, we have demonstrated that the efficiency of MAPI solar cells, based on mesoporous TiO<sub>2</sub>, not only depends on the MAPI itself as the photoactive material but also on the nature of the TiO<sub>2</sub> nanocrystalline particles that effects important changes on the interfacial charge transfer process that limit the solar cell efficiency.



## Acknowledgements

The authors thank MINECO (project CTQ2013-47183) as well as the Severo Ochoa Excellence Accreditation 2014–2018 (SEV-2013-0319). E.P. is also grateful to ICIQ and ICREA for economical support.

## References

- 1 P. P. Boix, K. Nonomura, N. Mathews and S. G. Mhaisalkar, *Mater. Today*, 2014, 17, 16–23.
- 2 P. Gao, M. Grätzel and M. K. Nazeeruddin, *Energy Environ. Sci.*, 2014, 7, 2448–2463.
- 3 K. T. Ramakrishna Reddy, N. Koteswara Reddy and R. W. Miles, *Sol. Energy Mater. Sol. Cells*, 2006, 90, 3041–3046.
- 4 H. Katagiri, K. Jimbo, W. S. Maw, K. Oishi, M. Yamazaki, H. Araki and A. Takeuchi, *Thin Solid Films*, 2009, 517, 2455–2460.
- 5 R. E. Smalley, *MRS Bull.*, 2004, 30, 412–417.
- 6 C. Kim, S. Ryu, J. Seo and S. I. Seok, *Science*, 2015, 348, 1234–1237.
- 7 S. D. Stranks and H. J. Snaith, *Nat. Nanotechnol.*, 2015, 10, 391–402.
- 8 K. Nakata and A. Fujishima, *J. Photochem. Photobiol., C*, 2012, 13, 169–189.
- 9 A. Haidry, P. Schlosser, P. Durina, M. Mikula, M. Tomasek, T. Plecenik, T. Roch, A. Pidik, M. Stefecka, J. Noskovic, M. Zahoran, P. Kus and A. Plecenik, *Cent. Eur. J. Phys.*, 2011, 9, 1351–1356.
- 10 S. Mathew, A. Yella, P. Gao, R. Humphry-Baker, F. E. Curchod, N. Ashari-Astani, I. Tavernelli, U. Rothlisberger, K. Nazeeruddin and M. Grätzel, *Nat. Chem.*, 2014, 6, 242–247.
- 11 B. O'Regan and M. Grätzel, *Nature*, 1991, 353, 737–740.
- 12 S. Hore, E. Palomares, H. Smit, N. J. Bakker, P. Comte, P. Liska, K. R. Thampi, J. M. Kroon, A. Hinsch and J. R. Durrant, *J. Mater. Chem.*, 2005, 15, 412–418.
- 13 F. Fabregat-Santiago, J. Garcia-Canadas, E. Palomares, J. N. Clifford, S. A. Haque, J. R. Durrant, G. GarciaBelmonte and J. Bisquert, *J. Appl. Phys.*, 2004, 96, 6903–6907.
- 14 E. Palomares, J. N. Clifford, S. A. Haque, T. Lutz and J. R. Durrant, *J. Am. Chem. Soc.*, 2003, 125, 475–482. 22160 | *J. Mater. Chem. A*, 2015, 3, 22154–22161
- 15 Q. Xue, Z. Hu, C. Sun, Z. Chen, F. Huang, H.-L. Yip and Y. Cao, *RSC Adv.*, 2015, 5, 775–783.
- 16 J. H. Heo, H. J. Han, D. Kim, T. K. Ahn and S. H. Im, *Energy Environ. Sci.*, 2015, 8, 1602–1608.

- 17 B. C. O'Regan, P. R. F. Barnes, X. Li, C. Law, E. Palomares and J. M. Marin-Beloqui, *J. Am. Chem. Soc.*, 2015, 5087–5099.
- 18 J.-H. Im, C.-R. Lee, J.-W. Lee, S.-W. Park and N.-G. Park, *Nanoscale*, 2011, 3, 4088–4093.
- 19 J. M. Marin-Beloqui, J. P. Hernandez and E. Palomares, *Chem. Commun.*, 2014, 50, 14566–14569.
- 20 K. Suttiponparnit, J. Jiang, M. Sahu, S. Suvachittanont, T. Charinpanitku and P. Biswas, *Nanoscale Res. Lett.*, 2011, 6, 1–8.
- 21 M. de Bastiani, V. D'Innocenzo, S. D. Stranks, H. J. Snaith and A. Petrozza, *APL Mater.*, 2014, 2, 081509.
- 22 V. Roiati, S. Colella, G. Lerario, L. de Marco, A. Rizzo, A. Listorti and G. Gigli, *Energy Environ. Sci.*, 2014, 7, 1889–1894.
- 23 Y. Yamada, T. Nakamura, M. Endo, A. Wakamiya and Y. Kanemitsu, *J. Am. Chem. Soc.*, 2014, 136, 11610–11613.
- 24 F. T. F. O'Mahony, Y. H. Lee, C. Jellett, S. Dmitrov, D. T. J. Bryant, J. R. Durrant, B. C. O'Regan, M. Graetzel, M. K. Nazeeruddin and S. A. Haque, *J. Mater. Chem. A*, 2015, 3, 7219–7223.
- 25 A. Marchioro, J. Teuscher, D. Friedrich, M. Kunst, R. van de Krol, T. Moehl, M. Grätzel and J.-E. Moser, *Nat. Photonics*, 2014, 8, 250–255.
- 26 R. Gottesman, L. Gouda, B. S. Kalanoor, E. Haltzi, S. Tirosh, E. Rosh-Hodesh, Y. Tischler, A. Zaban, C. Quarti, E. Mosconi and F. de Angelis, *J. Phys. Chem. Lett.*, 2015, 6, 2332–2338.
- 27 M. M. Lee, J. Teuscher, T. Miyasaka, T. N. Murakami and H. J. Snaith, *Science*, 2012, 338, 643–647.
- 28 J. Bisquert and G. Garcia-Belmonte, *J. Phys. Chem. Lett.*, 2011, 2, 1950–1964